

## Structural intensity assessment on shells *via* a finite element approximation

Felipe Pires, Stéphane Avril, Steve Vanlanduit, and Joris Dirckx

Citation: *The Journal of the Acoustical Society of America* **145**, 312 (2019); doi: 10.1121/1.5087564

View online: <https://doi.org/10.1121/1.5087564>

View Table of Contents: <https://asa.scitation.org/toc/jas/145/1>

Published by the [Acoustical Society of America](#)

---

### ARTICLES YOU MAY BE INTERESTED IN

[Acoustic perfect absorbers via Helmholtz resonators with embedded apertures](#)

*The Journal of the Acoustical Society of America* **145**, 254 (2019); <https://doi.org/10.1121/1.5087128>

[Improving sound transmission loss at ring frequency of a curved panel using tunable 3D-printed small-scale resonators](#)

*The Journal of the Acoustical Society of America* **145**, EL72 (2019); <https://doi.org/10.1121/1.5088036>

[Design and experimental investigation of V-folded beams with acoustic black hole indentations](#)

*The Journal of the Acoustical Society of America* **145**, EL79 (2019); <https://doi.org/10.1121/1.5088027>

[Acoustical boundary hologram for macroscopic rigid-body levitation](#)

*The Journal of the Acoustical Society of America* **145**, 328 (2019); <https://doi.org/10.1121/1.5087130>

[Parametric direction-of-arrival estimation with three recurrence relations of spherical harmonics](#)

*The Journal of the Acoustical Society of America* **145**, 480 (2019); <https://doi.org/10.1121/1.5087698>

[Demonstration of a quasi-monostatic autonomous underwater vehicle based high duty cycle active sonar](#)

*The Journal of the Acoustical Society of America* **145**, EL90 (2019); <https://doi.org/10.1121/1.5088029>

---



Advance your science and career  
as a member of the

ACOUSTICAL SOCIETY OF AMERICA

LEARN MORE



# Structural intensity assessment on shells *via* a finite element approximation

Felipe Pires,<sup>1,a)</sup> Stéphane Avril,<sup>2</sup> Steve Vanlanduit,<sup>3,b)</sup> and Joris Dirckx<sup>1</sup>

<sup>1</sup>Department of Physics, University of Antwerp, Groenenborgerlaan 171, Antwerp 2020, Belgium

<sup>2</sup>Mines Saint-Étienne, Université Lyon, INSERM, U 1059 Sainbiose, Centre CIS, F, Saint-Étienne 42023, France

<sup>3</sup>Department of Electromechanical Engineering, University of Antwerp, Groenenborgerlaan 171, Antwerp 2020, Belgium

(Received 1 July 2018; revised 21 November 2018; accepted 18 December 2018; published online 22 January 2019)

Structural intensity on plates or shells can provide insights on how the vibrational energy is transmitted throughout a sample. Its assessment via experimental deflections are widely documented in the case of plates, which just requires the computation of spatial derivatives of out-of-plane displacements or velocities and a knowledge of the sample's material properties. However, if the structural intensity is to be assessed on arbitrary shells, a more elaborate data processing is required. The in-plane displacements become relevant terms and the spatial derivatives along a predefined local coordinate system need to be computed. Here, a method from which experimental data is interpolated on a finite element mesh is proposed. First, the global displacements and shape of a sample's outer-surface are measured. These data are then projected on a quadratic mesh, where the Kirchhoff plate theory is invoked for the individual elements. The data differentiation is computed via quadratic shape functions, from which the strains and structural intensity are estimated. Through the obtained vibrational energy results on the basis of measured displacement and shape data and by validating the method via a numerical simulation, the proposed work has shown to be a reliable tool to assess energy transmission on irregular shells.

© 2019 Acoustical Society of America. <https://doi.org/10.1121/1.5087564>

[KW]

Pages: 312–326

## I. INTRODUCTION

Structural intensity (SI) analysis describes the magnitude and direction of vibrational energy being transported by elastic waves in a structure. Such a tool was widely used to analyze dominant transmission paths, energy dissipation, and source localization in both experimental and numerical studies.

When experimental data of plate-like structures are analyzed, it is convenient to invoke the Kirchhoff-Love postulates (Miguel and Feit, 1986), so the SI can be assessed in terms of the out-of-plane and full-field displacements or velocities and *a priori* knowledge of the sample's material properties. The quality of the computed energy transmission strongly depends on the signal-to-noise ratio of the experimental deflections, on the amount of measurement points, and the employed differentiation technique to estimate the strains and generalized forces.

All these aspects have been improved since the pioneering works regarding the SI assessments via the use of accelerometers during the 1970s (Noiseux, 1970; Pavić, 1976). Later on, non-contact measurement techniques permitted the

deflections' assessment on denser grids. Examples of reported methods to analyze the vibrational energy are the laser Doppler vibrometry (Arruda and Mas, 1998; Morikawa *et al.*, 1996; Pascal *et al.*, 2002; Pascal *et al.*, 2006; Roozen *et al.*, 2015; Schmidt, 2009; Vuye, 2011; Zhang and Mann, 1996), acoustic-holography (Pascal *et al.*, 1990; Saijyou, 2007), electronic speckle interferometry (Eck and Walsh, 2012), holographic interferometry (Pascal *et al.*, 1996), and digital stroboscopic holography (Pires *et al.*, 2018).

The differentiation of the experimental data has been performed mainly by the finite difference method (Arruda and Mas, 1998; Schmidt, 2009) or by processing and filtering the data in its corresponding wavenumber domain (Arruda, 1992; Lopes *et al.*, 2006; Morikawa *et al.*, 1996; Pascal *et al.*, 1996; Pascal *et al.*, 2002; Pascal *et al.*, 2006). Such approaches to assess the required spatial derivatives in combination with the described measuring techniques provided meaningful insights in the field, which includes the analysis of plates with peculiar features, such as plates with ribs or joints (Pascal *et al.*, 2006; Semperlotti and Conlon, 2010; Zhang and Mann, 1996), with cracks (Schmidt, 2009) and with orthotropic material properties (Lamberti and Semperlotti, 2013).

Apart from the SI assessment via experimental data, the use of numerical simulations has also proven to be a useful tool. This approach was not just used to analyze the energy transmission on plates, but also on general structures with irregular shapes. The geometries of interest are mainly developed as finite element (FE) models by using solid

<sup>a)</sup>Also at: Department of Mechanical Engineering, Vrije Universiteit Brussel, Pleinlaan 2, Brussels 1050, Belgium. Electronic mail: felipe.pires@uantwerpen.be

<sup>b)</sup>Also at: Department of Mechanical Engineering, Vrije Universiteit Brussel, Pleinlaan 2, Brussels 1050, Belgium.

(Hambric and Szwerc, 1999; Shepherd *et al.*, 2012; Xu *et al.*, 2004a) or shell elements (Gavrić and Pavić, 1993; Hambric, 1990; Lee *et al.*, 2006; Li and Lai, 2000; Liu *et al.*, 2005; Petrone *et al.*, 2016; Xu *et al.*, 2004b). A variety of works were reported in literature, such as the SI study on cracks present in ships or off-shore platforms (Cho *et al.*, 2010; Tian *et al.*, 2017), of locally resonant metamaterials (Al Ba'ba'a *et al.*, 2018; Al Ba'ba'a and Nouh, 2017) and of stiffened or ribbed plates (Cho *et al.*, 2018; Schaal *et al.*, 2016; Xu *et al.*, 2005). Other numerical examples have been also developed to assess the SI on plates containing geometrical or constitutive heterogeneities, such as the case of stepped thickness plates (Cho *et al.*, 2016) and samples with orthotropic material properties (Lamberti and Semperlotti, 2013; Petrone *et al.*, 2016; Tran *et al.*, 2007; Xu *et al.*, 2004b).

However, in spite of the advancements in this field, just a few studies regarding the SI on shell-like structures have been developed (Saijyou, 2007; Williams, 1991). Moreover, the SI terms from such samples are conveniently formulated if a set of curvilinear coordinate system is chosen to represent the shell's behavior from its mid-surface (Gavrić and Pavić, 1993). If this approach is chosen, then the spatial derivatives along these very coordinates need to be carried out, so the strains and, in turn, the SI vector components can be retrieved. From these requirements, it can be noted that the definition of these local coordinates depend on the shape of the analyzed sample. Since the in-plane displacement components are no longer negligible (Cho *et al.*, 2010; Gavrić and Pavić, 1993; Romano *et al.*, 1992; Romano *et al.*, 1990; Zhang, 1993), full-field experimental data along three orthonormal directions need to be measured. Such demands were not present for the case of plates, whose analyses were just based on the measurement of out-of-plane displacement or velocity fields and whose differentiation could be carried out along a predefined Cartesian coordinate system. Besides, the attempts made so far to analyze the SI on the basis of curvilinear coordinates were restricted to analytical ones, such as the cylindrical or the spherical coordinates (Romano *et al.*, 1990; Saijyou, 2007; Williams, 1991; Zhang, 1993).

Apart from these limitations, the standard non-contact measurement techniques cited above are just able to extract data from a sample's outer-surface. Since the displacements may vary with respect to a shell's thickness, extra steps and proper assumptions need to be taken into account, so the information at the mid-surface can be estimated from the provided data at the sample's outer-surface.

It is the aim of this paper to present a method that tackles the mentioned issues regarding the SI assessment on irregular shells by projecting the experimental data to a FE mesh (Avril *et al.*, 2009; Feng and Rowlands, 1991). The chosen non-contact measurement technique was the Digital Image Correlation (DIC) (Schreier *et al.*, 2009), since it computes both data of interest for this application, i.e., the spatial coordinates describing the shape of the sample's outer-surface and associated displacement data in all three orthonormal directions.

By invoking proper assumptions and approximations, the projected displacements are represented on the basis of a local coordinate system, so all necessary differentiations are computed by choosing proper FE shape functions. The processed data from the outer-surface were then used as input to identify the fields on the mid-surface and the SI was assessed.

All computed SI results showed energy transmission paths that were expected from the analyzed sample. The assessed vector fields of vibrational energy strongly converged to a region on the sample where a viscous damper was installed. Additionally, the accuracy of the data processing proposed in this paper was also tested with the results of a FE shell model. The SI outputs that were acquired via the proposed method and the one provided by the numerical simulation showed similar energy transmission patterns both in magnitude and direction. Due to these findings and by validating this work via a simulation, it is suggested that the current method can handle the major difficulties regarding the SI assessment on arbitrary shells.

## II. THEORY

### A. Structural intensity

It is the aim of this work to assess and visualize the energy paths taking place on irregular shells. This data is defined as the product of the vibration particle velocity and stress tensor (Morse and Feshbach, 1946; Zhang, 1993), which are quantities that are not directly measurable on general structures. However, these two terms can be related to the displacements, rotations, and generalized forces by making assumptions. By invoking the Kirchoff-Love postulates (Miguel and Feit, 1986), the time-averaged and active SI per unit length [ $\text{W m}^{-1}$ ] of a shell under harmonic motion is

$$\mathbf{I} = \mathbf{I}_Q + \mathbf{I}_M + \mathbf{I}_N, \quad (1)$$

where

$$\mathbf{I}_Q = -(\pi f) \begin{Bmatrix} \Im\{Q_1 u_3^*\} \\ \Im\{Q_2 u_3^*\} \\ 0 \end{Bmatrix}, \quad (2)$$

$$\mathbf{I}_M = -(\pi f) \begin{Bmatrix} \Im\{M_{11} a_1^* + M_{12} a_2^*\} \\ \Im\{M_{21} a_1^* + M_{22} a_2^*\} \\ 0 \end{Bmatrix}, \quad (3)$$

$$\mathbf{I}_N = -(\pi f) \begin{Bmatrix} \Im\{N_{11} u_1^* + N_{12} u_2^*\} \\ \Im\{N_{21} u_1^* + N_{22} u_2^*\} \\ 0 \end{Bmatrix}. \quad (4)$$

Here,  $f$  is the frequency at which the structure vibrates, the superscript “\*” is the complex conjugate symbol, and “ $\Im\{\}$ ” indicates that only the imaginary part of the referred term should be taken into account. The first and second rows of the vectors  $\mathbf{I}_Q$ ,  $\mathbf{I}_M$ , and  $\mathbf{I}_N$  [Eqs. (2)–(4)] point at directions that are always tangent to the surface of the analyzed shell,

while the third row indicates the normal direction of the surface.

Besides, the subscripts “1” and “2” in these equations indicate the directions of the two tangent coordinates, and the subscript “3” indicates the perpendicular one. The defined triad (“1” to “3”) correspond to an orthogonal and local coordinate system, which is defined here as  $(\mathbf{e}_1, \mathbf{e}_2, \mathbf{e}_3)$ . Hence, the unit vectors  $\mathbf{e}_1$  and  $\mathbf{e}_2$  are always tangent to the shell’s surface and the vector  $\mathbf{e}_3$  is aligned with the through-thickness coordinate.

The terms related to  $u$  are the scalar components of the displacements on the mid-surface;  $a$  refers to the rotations about the normals to that very surface. The parameters indicated with the letters  $Q$ ,  $N$ , and  $M$  are referenced here as the generalized forces taking place on the shell and are the scalar components of the shear force  $\mathbf{Q}$ , the membrane force  $\mathbf{N}$ , and the bending moment  $\mathbf{M}$ , respectively. The development of the equations that relate the generalized forces with displacements or rotations can acquire convenient forms if proper assumptions are used. The next section (Sec. II B) presents these simplifications, from which  $\mathbf{Q}$ ,  $\mathbf{M}$ , and  $\mathbf{N}$  are derived.

## B. Kirchhoff-Love plate model

As it is evident from the experiment described in Sec. III, the only recorded information from the sample are its shape and displacement fields on its outer-surface. The energy transmission shown in Eqs. (1)–(4), on the other hand, are defined on a shell’s mid-surface. The relation between the data described in both surfaces depends on the assumptions describing the analyzed sample. To this end, it is assumed that the shell under study can be represented as an assembly of elements whose mid-surfaces are planar and whose behavior can be predicted by the Kirchhoff plate theory.

Since the individual elements are considered to be flat, their curvatures are set to zero and the second and third fundamental forms vanish from the equations relating the displacements and rotations with the strains (Chapelle and Bathe, 2010). Moreover, the Kirchhoff plate theory permits the rotation to be estimated directly from the outer-surface, since this parameter is assumed to be independent from the through-thickness coordinate. The assumed theory also permits the relations between the data from the outer-surface and energy transmission from the mid-surface to be conveniently developed, since the displacements and strains vary linearly with respect to the shell’s normal direction. Due to all these simplifications, the generalized forces acquire relatively simpler forms and can be estimated on the basis of data recorded from a sample’s outer-surface.

### 1. Kinematics of shells

The equations supporting the proposed data processing of this work are entirely based on the Kirchhoff-Love plate model for shells; which, in turn, obeys the Kirchhoff-Love postulates (Miguel and Feit, 1986). By recalling the assumption that the shell’s normal direction undergoes no change in length during deformation (Kraus, 1967), one can state that the displacement has a linear distribution in its normal

direction (Bischoff and Ramm, 1997; Büchter *et al.*, 1994) and the following relation holds:

$$\mathbf{u}^{h/2} = \mathbf{u} + \frac{h}{2}\mathbf{a}, \quad (5)$$

where  $\mathbf{u}$  is the displacement vector field at the mid-surface of the shell,  $\mathbf{a}$  is the rotation about the normal to that very surface,  $h$  is the thickness value of the shell, and the  $\mathbf{u}^{h/2}$  is the displacement on the outer-surface.

As it was the case for Eq. (1), the scalar components of  $\mathbf{u}^{h/2}$ ,  $\mathbf{u}$ , and  $\mathbf{a}$  also correspond to the orthogonal coordinate system  $(\mathbf{e}_1, \mathbf{e}_2, \mathbf{e}_3)$ . Hence

$$\mathbf{u}^{h/2} = \begin{Bmatrix} u_1^{h/2} \\ u_2^{h/2} \\ u_3^{h/2} \end{Bmatrix}, \quad \mathbf{u} = \begin{Bmatrix} u_1 \\ u_2 \\ u_3 \end{Bmatrix}, \quad \mathbf{a} = \begin{Bmatrix} a_1 \\ a_2 \\ 0 \end{Bmatrix}, \quad (6)$$

where the in-plane directions of the displacements and rotations are indicated by the subscript “1” and “2,” and the subscript “3” indicates the scalar field along the out-of-plane direction.

By recalling the assumptions of the Kirchhoff-Love plate model once again, one can relate the linearized Green-Lagrange strain on the outer-surface  $\boldsymbol{\varepsilon}^{h/2}$  as a function of the membrane and bending strains (Chapelle and Bathe, 2010), i.e.,

$$\boldsymbol{\varepsilon}^{h/2} = \boldsymbol{\gamma} + \frac{h}{2}\boldsymbol{\chi}, \quad (7)$$

where  $\boldsymbol{\gamma}$  is the membrane strain and  $\boldsymbol{\chi}$  is the bending strain linearly varying over the shell’s thickness. The scalar components of the vectors in Eq. (7) are

$$\boldsymbol{\varepsilon}^{h/2} = \begin{Bmatrix} \varepsilon_{11}^{h/2} \\ \varepsilon_{22}^{h/2} \\ \varepsilon_{12}^{h/2} \end{Bmatrix}, \quad \boldsymbol{\gamma} = \begin{Bmatrix} \gamma_{11} \\ \gamma_{22} \\ \gamma_{12} \end{Bmatrix}, \quad \boldsymbol{\chi} = \begin{Bmatrix} \chi_{11} \\ \chi_{22} \\ \chi_{12} \end{Bmatrix}. \quad (8)$$

By knowing that the elements describing the assembly are planar, the strains  $\boldsymbol{\varepsilon}^{h/2}$  and  $\boldsymbol{\chi}$  can be interpreted as functions of the displacement and rotation being differentiated along the local coordinates  $\mathbf{e}_1$  and  $\mathbf{e}_2$ . Hence

$$\varepsilon_{ij}^{h/2} = \frac{1}{2}(u_{i,j}^{h/2} + u_{j,i}^{h/2}), \quad \text{for } i, j = \{1, 2\}, \quad (9)$$

and

$$\chi_{ij} = \frac{1}{2}(a_{i,j} + a_{j,i}), \quad \text{for } i, j = \{1, 2\}, \quad (10)$$

where the subscripts “ $i$ ” or “ $j$ ” indicate that the fields are differentiated along the directions “ $i$ ” or “ $j$ ,” respectively.

### 2. Generalized forces

Since the strains’ formulations are available, the non-negligible stress components can be defined as functions of

the strain varying linearly with respect to the through-thickness coordinate  $\zeta$  and the shell's material properties. Therefore, it follows that

$$\boldsymbol{\sigma}^\zeta = \Omega \boldsymbol{\varepsilon}^\zeta, \quad (11)$$

where  $\Omega$  is the stiffness matrix,  $\boldsymbol{\sigma}^\zeta$  is the stress as a function of the through-thickness coordinate  $\zeta$ , and  $\boldsymbol{\varepsilon}^\zeta$  is the Green-Lagrange strain as a function of  $\zeta$ . These parameters are defined as

$$\Omega = \frac{E}{1-\nu^2} \begin{bmatrix} 1 & \nu & 0 \\ \nu & 1 & 0 \\ 0 & 0 & 1-\nu \end{bmatrix}, \quad (12)$$

$$\boldsymbol{\sigma}^\zeta = \begin{Bmatrix} \sigma_{11}^\zeta \\ \sigma_{22}^\zeta \\ \sigma_{12}^\zeta \end{Bmatrix}, \quad \boldsymbol{\varepsilon}^\zeta = \begin{Bmatrix} \varepsilon_{11}^\zeta \\ \varepsilon_{22}^\zeta \\ \varepsilon_{12}^\zeta \end{Bmatrix}. \quad (13)$$

By integrating Eq. (11) with respect to the through-thickness coordinate  $\zeta$ , the generalized forces related to the membrane strain  $\boldsymbol{\gamma}$  and the bending strain  $\boldsymbol{\chi}$  can be computed

$$\mathbf{N} = h\Omega\boldsymbol{\gamma}, \quad (14)$$

$$\mathbf{M} = \frac{h^3}{12}\Omega\boldsymbol{\chi}, \quad (15)$$

being the components of the membrane force  $\mathbf{N}$  and bending moment  $\mathbf{M}$  defined as

$$\mathbf{N} = \begin{Bmatrix} N_{11} \\ N_{22} \\ N_{12} \end{Bmatrix}, \quad \mathbf{M} = \begin{Bmatrix} M_{11} \\ M_{22} \\ M_{12} \end{Bmatrix}, \quad (16)$$

and where

$$M_{21} = M_{12}, \quad N_{21} = N_{12}, \quad (17)$$

from Novozhilov (1959) and by considering the current case of a Kirchhoff-Love plate model (Chapelle and Bathe, 2010).

The internal forces related to the shear force  $\mathbf{Q}$  are assessed by analyzing the equilibrium conditions of a differential element and by taking into account that the shell is being represented by an assembly of plates. Through the equilibrium conditions, the shear force acquires the following form (Ventsel and Krauthammer, 2001):

$$\mathbf{Q} = \begin{Bmatrix} Q_1 \\ Q_2 \end{Bmatrix} = \begin{Bmatrix} M_{11,1} + M_{12,2} \\ M_{12,1} + M_{22,2} \end{Bmatrix}. \quad (18)$$

It can be noted from Eq. (18) that the shear force is dependent on the spatial derivatives of the bending moment. If the scalar components of Eq. (15) are differentiated, it holds that

$$M_{ii,i} = \frac{h^3}{12} \frac{E}{1-\nu^2} (\chi_{ii,i} + \nu\chi_{jj,i}), \quad \text{for } i,j = \{1,2\}, \quad (19)$$

$$M_{ij,i} = \frac{h^3}{12} \frac{E}{1+\nu} \chi_{ij,i}, \quad \text{for } i,j = \{1,2\}. \quad (20)$$

The derivatives of  $\chi_{ij}$  in Eqs. (19) and (20) can be acquired by differentiating the bending strain  $\boldsymbol{\chi}$  in Eq. (10)

$$\chi_{ij,i} = \frac{1}{2}(a_{i,ij} + a_{j,ii}), \quad \text{for } i,j = \{1,2\}, \quad (21)$$

where  $\chi_{ij,i}$  is a scalar component of  $\boldsymbol{\chi}_{,i}$ . From the derivations shown in Eqs. (18)–(21), it is clear that in order to access  $\mathbf{Q}$ , the second order derivatives of the rotation (presented throughout this work as  $\mathbf{a}_{,ij}$ ) are required.

### 3. Assessment of data on the mid-surface

The equations provided so far are given to support the processing from the data available at the outer-surface of a sample, i.e., the terms  $\mathbf{u}^{h/2}$  and  $\mathbf{a}$  from Eq. (5); and  $\boldsymbol{\varepsilon}^{h/2}$  and  $\boldsymbol{\chi}$  from Eq. (7). By analyzing the SI scalar components in Eqs. (2)–(4), it can be noted that the terms related to the displacement on the mid-surface  $\mathbf{u}$  would still be missing. Moreover, the membrane force  $\mathbf{N}$  cannot be directly estimated, since it is formulated as a function of the membrane strain  $\boldsymbol{\gamma}$ , which is also a parameter from a shell's mid-surface.

The approach used to assess both the displacement  $\mathbf{u}$  and the membrane strain  $\boldsymbol{\gamma}$  was simply to isolate these very terms from Eqs. (5) and (7). By assuming that one has a previous knowledge of all other terms, the displacement and strain on the mid-surface can be recovered from

$$\mathbf{u} = \mathbf{u}^{h/2} - \frac{h}{2}\mathbf{a}, \quad (22)$$

and

$$\boldsymbol{\gamma} = \boldsymbol{\varepsilon}^{h/2} - \frac{h}{2}\boldsymbol{\chi}. \quad (23)$$

If the term  $\boldsymbol{\chi}_{,i}$  is also at hand, all generalized forces ( $\mathbf{N}$ ,  $\mathbf{M}$  and  $\mathbf{Q}$ ) can be assessed from Eqs. (14), (15), (18)–(20) and it is possible to estimate the SI on the basis of Eqs. (1)–(4).

By adopting the Kirchhoff-Love plate model to represent a real sample, one can also state that such an assembly can be treated as a FE mesh, whose local Degrees of Freedom (DoFs) are the displacement  $\mathbf{u}$  and rotation  $\mathbf{a}$  [Eq. (5)]. By choosing proper shape functions, these DoFs can be differentiated along the directions  $\mathbf{e}_1$  and  $\mathbf{e}_2$  [Eqs. (9), (10), (21)] and the generalized forces can be assessed.

However, as it will be pointed out in Sec. III, the experimental displacements from the outer-surface that are exported from the developed set-up are defined on a Cartesian coordinate system ( $\mathbf{e}_x$ ,  $\mathbf{e}_y$ ,  $\mathbf{e}_z$ ) (defined throughout this work as  $\mathbf{U}_{exp}^{h/2}$ ). Moreover, the spatial coordinates of the FE mesh's nodes are usually not equal in number or position with the coordinates from which the experimental data  $\mathbf{U}_{exp}^{h/2}$  is recorded.

Due to these two issues, the measurements need to be first projected from the dense experimental point cloud to the nodes of a mesh and then a transformation of coordinate

systems needs to take place. Both issues are addressed in detail in Secs. II C and II E, respectively.

### C. Data projection on a finite element mesh

It can be noted from Sec. II B 2 that in order to assess  $\mathbf{Q}$ ,  $\mathbf{N}$ , and  $\mathbf{M}$ ; first order derivatives of  $\mathbf{u}$  [Eq. (9)] and second order derivatives of  $\mathbf{a}$  [Eq. (21)] need to be computed. This work proposes the processing of these spatial derivatives via FE shape functions.

It follows that a generalized vector field  $\hat{\psi}$  can be calculated at any position  $\mathbf{x}$  within an element by interpolating the information stored at its nodes and predefined shape functions  $N$ . Therefore, it holds that

$$\hat{\psi}(\mathbf{x}) = \sum_{b=1}^c N_b(\mathbf{x}) \cdot \tilde{\psi}_b, \quad (24)$$

being “ $c$ ” the total number of nodes present in an FE element,  $\tilde{\psi}$  is a generalized DoF stored on the mesh’s nodes, and the subscript “ $b$ ” depicts the node numbering of the field  $\tilde{\psi}$  and the shape function  $N$ .

The approach used to perform the projection of experimental data on a mesh was the global least-squares minimization via FE shape functions (Avril *et al.*, 2009; Avril and Pierron, 2007; Feng and Rowlands, 1991) over the whole sample’s measurement domain. The minimization problem is defined as

$$\min \sum_{a=1}^d |\hat{\psi}(\mathbf{x}_a) - \psi(\mathbf{x}_a)|^2, \quad (25)$$

where  $\psi$  refers to a generalized experimental data and  $d$  is the total number of evaluated points of  $\psi$ . By substituting  $\hat{\psi}$  with the right-handed terms of Eq. (24) and by considering  $\Phi$ ,  $\tilde{\Psi}$ , and  $\Psi$ , the assembled matrices of  $N(\mathbf{x}_a)$ ,  $\tilde{\psi}(\mathbf{x}_a)$ , and  $\psi(\mathbf{x}_a)$ , respectively, Eq. (25) can be represented in its assembled matrix form as

$$\tilde{\Psi} = \left[ [\Phi^T \Phi]^{-1} \Phi^T \right] \Psi. \quad (26)$$

From here, it becomes evident that the measured full-field data  $\Psi$ , their corresponding spatial coordinates  $\mathbf{x}_a$  and defined basis functions  $N(\mathbf{x}_a)$  are sufficient inputs to solve the minimization problem. At the end of this process, one has access to the assembled data  $\tilde{\Psi}$  at the nodal points of a FE mesh.

In the current work, the experimental displacements  $\mathbf{U}_{exp}^{h/2}$  and related spatial coordinates  $\mathbf{x}$  on the outer-surface are the data that will be projected on the mesh. If these two terms are available, one has all the necessary inputs of Eq. (26), so the projection procedure can take place on the mesh. By substituting  $\Psi$  with  $\mathbf{U}_{exp}^{h/2}$  in Eq. (26), it is concluded that

$$\tilde{\mathbf{U}}^{h/2} = \left[ [\Phi^T \Phi]^{-1} \Phi^T \right] \mathbf{U}_{exp}^{h/2}, \quad (27)$$

being  $\tilde{\mathbf{U}}^{h/2}$  the displacements of the outer-surface and stored on the mesh’s nodes.

### D. Assessment of rotations

Since the Kirchhoff plate theory is being imposed on the shell’s elements, the rotation at each node can be computed by subtracting the normal directions of the mesh under its deformed configuration with the ones in the reference configuration (Bischoff and Ramm, 1997; Murthy and Gallagher, 1986; Wagner and Gruttmann, 1994). Moreover, due to the assumption stating that the normal direction of the mid-surface remains perpendicular to that very surface after deformation, the subtraction’s result becomes independent from the local coordinate  $\zeta$ . Hence, this operation can be done at  $\zeta = h/2$ , which is the region where the experimental data are extracted from.

By assuming that the term  $\tilde{\mathbf{U}}^{h/2}$  and the mesh are at hand, the rotation corresponding to the stationary Cartesian coordinate system ( $\tilde{\mathbf{A}}$ ) can be assessed. This is achieved by subtracting the normal directions of the mesh at its deformed state ( $\mathbf{n}_{def}$ ) from its reference state ( $\mathbf{e}_3$ ). The deformed state of the mesh is computed by translating the nodes at the direction provided by the displacements  $\tilde{\mathbf{U}}^{h/2}$ . The unit vectors  $\mathbf{n}_{def}$  are then computed and the subtraction can take place. Therefore, it holds that

$$\tilde{\mathbf{A}} = \mathbf{n}_{def} - \mathbf{e}_3. \quad (28)$$

By accomplishing this step, each node of the FE mesh should have six DoFs that are aligned with ( $\mathbf{e}_x$ ,  $\mathbf{e}_y$ ,  $\mathbf{e}_z$ ): three scalar components of  $\tilde{\mathbf{U}}^{h/2}$  and the other three of  $\tilde{\mathbf{A}}$ .

### E. Coordinate system transformation and data differentiation

As pointed out in Sec. II B 3, the computation of Eqs. (2)–(4) requires that the displacement and rotation be aligned with the local triad ( $\mathbf{e}_1$ ,  $\mathbf{e}_2$ ,  $\mathbf{e}_3$ ). With previous knowledge of these coordinates, the orthonormal basis representing  $\tilde{\mathbf{U}}^{h/2}$  and  $\tilde{\mathbf{A}}$  are rotated accordingly in each element and their components in the local coordinates are obtained. These terms are denoted here as  $\tilde{\mathbf{u}}^{h/2}$  and  $\tilde{\mathbf{a}}$ , and are also stored on the mesh’s nodes.

It was stated previously that second order derivatives of  $\mathbf{a}$  need to be computed to access the shear forces [Eqs. (18)–(21)]. Therefore, the Kirchhoff-Love plate model requires at least quadratic shape functions, so this higher-order differentiation can be processed.

The proposed work makes use of triangular elements to develop the FE mesh, since it is the most popular element for estimating in-plane related variables (Dhatt *et al.*, 1986) and is capable of discretizing arbitrary shells efficiently. By applying quadratic shape functions on this assembly, it holds that the FE mesh is built upon a collection of six-noded triangles (Zienkiewicz *et al.*, 1977), i.e., linear-strain triangular elements (LST).

By defining that each element has six nodes and by substituting  $\tilde{\psi}$  for either  $\tilde{\mathbf{u}}^{h/2}$  or  $\tilde{\mathbf{a}}$  in Eq. (24), it holds that

$$\hat{\mathbf{u}}^{h/2}(\mathbf{x}) = \sum_{b=1}^6 N_b(\mathbf{x}) \cdot \tilde{\mathbf{u}}_b^{h/2}, \quad \hat{\mathbf{a}}(\mathbf{x}) = \sum_{b=1}^6 N_b(\mathbf{x}) \cdot \tilde{\mathbf{a}}_b, \quad (29)$$

where  $\hat{\mathbf{u}}^{h/2}$  and  $\hat{\mathbf{a}}$  are the displacement and rotation being evaluated at the position  $\mathbf{x}$  inside an element.

For the purpose of this work, it was decided to evaluate the shell's behavior at the barycentric coordinates of the FE mesh's elements. Hence, by defining  $\bar{N}$  to be the shape functions being evaluated at these very coordinates and by substituting them into Eq. (29)

$$\mathbf{u}^{h/2} = \sum_{b=1}^6 \bar{N}_b \cdot \tilde{\mathbf{u}}_b^{h/2}, \quad \mathbf{a} = \sum_{b=1}^6 \bar{N}_b \cdot \tilde{\mathbf{a}}_b, \quad (30)$$

being  $\mathbf{u}^{h/2}$  and  $\mathbf{a}$  the terms present in Eq. (5).

As it is the case for the left-handed terms of Eq. (30), their spatial derivatives are also estimated on the barycenter of the elements. It could be seen from Eqs. (9) and (21) that first order derivatives of  $\mathbf{u}^{h/2}$  and second order derivatives of  $\mathbf{a}$  are required for the SI assessment Eqs. (2) and (4).

By differentiating the shape functions terms in Eq. (30) to the demanded differentiation orders, it holds that

$$\mathbf{u}_{,i}^{h/2} = \sum_{b=1}^6 \bar{N}_{b,i} \cdot \tilde{\mathbf{u}}_b^{h/2}, \quad (31)$$

$$\mathbf{a}_{,i} = \sum_{b=1}^6 \bar{N}_{b,i} \cdot \tilde{\mathbf{a}}_b, \quad \mathbf{a}_{,ij} = \sum_{b=1}^6 \bar{N}_{b,ij} \cdot \tilde{\mathbf{a}}_b, \quad (32)$$

where the terms  $\mathbf{u}_{,i}^{h/2}$ ,  $\mathbf{a}_{,i}$  and  $\mathbf{a}_{,ij}$  are spatial derivatives along the local directions “ $i$ ” or “ $j$ ” and which are present in Eqs. (9), (10), and (21). By making use of the Eqs. (30)–(32), the strains and related derivatives  $\boldsymbol{\varepsilon}^{h/2}$ ,  $\boldsymbol{\chi}$ , and  $\boldsymbol{\chi}_{,i}$  [Eqs. (9), (10), (21)] can be also assessed. From these terms, the fields related to the element's mid-surfaces  $\mathbf{u}$  and  $\boldsymbol{\gamma}$  are estimated via the Eqs. (22) and (23) and from which all generalized forces [Eqs. (14), (15), (18)–(20)] and, in turn, the SI [Eqs. (1)–(4)] can be computed.

### III. MATERIALS

The measurement of full-field displacements and subsequent data processing was performed on a circular membrane made of silicon, whose boundaries were fixed (Fig. 1). Its Young's modulus  $E$  was estimated to be 8 MPa through a tensile test, its Poisson's coefficient  $\nu$  was assumed to be 0.3, and its thickness and diameter were 1 mm and 12 cm, respectively.

The device that disturbed this specimen was a loudspeaker (TOA Corporation, TU-650, Tokyo, Japan). The delivered excitation pressure was set to a single frequency, while a full-field displacement measurement was being performed. Since it was desired to visualize energy paths of the

SI on the silicon membrane, a strip of a synthetic viscoelastic urethane polymer (Thorlabs, SB12B Sorbothane Sheet, Newton, NJ) was fixed from one of its extreme sides with the center of the membrane, so the power being provided by the loudspeaker would be absorbed on that region (depicted as “damper” in the cross-section view of Fig. 1). The region between the loudspeaker and the membrane was isolated in a chamber to ensure that most of the delivered power would be directed to the specimen.

Since the final aim of this work is to process displacement and shape data on irregular shells, the manipulation of the membrane's shape was accomplished by moving the other extreme end of the polymer strip. By pulling this material, the membrane would gradually obtain a curved-conical shape in its reference configuration.

To avoid the presence of pre-strains in the resting position by excessively pulling the damper, the membrane's boundaries were clamped in such a way that membrane would not be stretched at first, leaving it loose and with “wrinkles.” Afterwards, the viscous polymer was attached to the membrane's surface from the chamber's interior.

The polymer was then carefully pulled from its free end and from inside the chamber. The pulling of the damper would stop at the moment where the membrane's “wrinkles” would cease to exist. This qualitative and visual calibration would indicate that the specimen would be on the verge of having residual strains if the damper would be further pulled. At the end of this process, the free end of the polymer was fixed and the curved-conical shape of the membrane would be acquired. Moreover, the outer-surface of the membrane was sprayed on with a black-acrylic ink and a fine speckle pattern was drawn on its surface.

The measurement of membrane's spatial coordinates at its resting configuration ( $\mathbf{x}$ ) and densely distributed displacement measurements on that surface were obtained via the DIC technique (Schreier *et al.*, 2009). For this aim, a Q-400 digital three-dimensional image correlation system provided by Dantec/Limess was used. The membrane's dynamic behavior was captured by two high-speed camera's (see Fig. 1) and the images' evaluation was carried out by the Istra4D software provided by the system.

The normalization of the displacement and processed data was calculated by using the excitation pressure as references. This parameter was measured by a probe microphone (Brüel & Kjær, type 4182, Nærum, Denmark), which was installed inside the chamber. The device was fixed near the membrane and the distance between its tip and the specimen was approximately 2 mm.

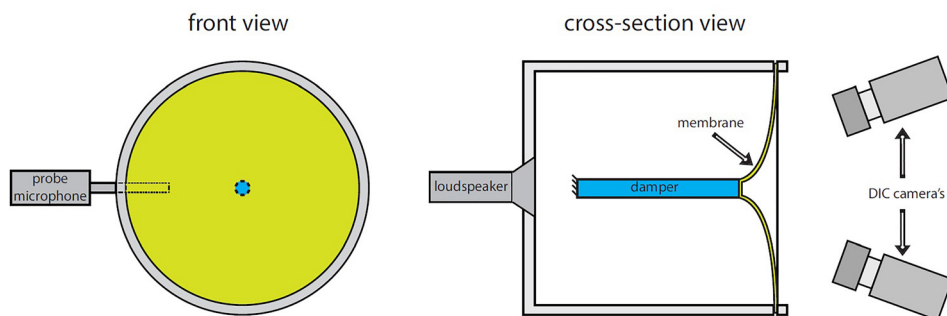


FIG. 1. (Color online) Set-up configuration.

The computation of the shape's spatial coordinates and normalized displacement were carried out under several excitation frequencies. To ensure that the harmonic excitation pressure would be uniform throughout the membrane's surface, it was decided to perform the dynamic analysis on low excitation frequencies only (ranging from 60 Hz up to 170 Hz).

As it was already mentioned, second order spatial derivatives of the data need to be computed, and the quality of these differentiations are highly dependent on the signal-to-noise ratio of the measured displacement fields. Therefore, it has been decided to filter the displacement fields to ensure that the influence of noise is diminished before the data projection on a mesh. The chosen approach for this work was to apply an in-house Gaussian filter with a standard deviation of 1 on every displacement field. From now on, these filtered global displacement fields are referenced here as the term  $\mathbf{U}_{exp}^{h/2}$ , which was cited in Sec. II C and in Eq. (27).

After performing the measurements on the circular membrane, the terms  $\mathbf{U}_{exp}^{h/2}$  and  $\mathbf{x}$  are obtained. These two groups of experimental parameters were then used to assess the SI under different excitation frequencies. The procedure from which the energy transmission paths are computed from  $\mathbf{U}_{exp}^{h/2}$  and  $\mathbf{x}$  are described in the following section (Sec. IV).

## IV. METHODS

### A. Measurements via the DIC technique

After preparing the set-up described in Sec. III, the circular membrane was disturbed by the loudspeaker under several excitation frequencies ranging from 60 to 170 Hz. The high-speed camera's captured the membrane's motion and the recorded images were correlated with the support of the Istra4D software.

The spatial coordinates of the membrane in its resting configuration  $\mathbf{x}$  could then be generated and full-field displacements  $\mathbf{U}_{exp}^{h/2}$  of that sample were computed in several frequencies. At the end of this step, both groups of data were exported for further processing.

### B. Mesh generation and definition of the local coordinate system

By possessing the data  $\mathbf{x}$ , it is feasible to create a mesh whose shape would overlap the original spatial coordinates of the membrane. As it was pointed out in Sec. II E, the current application requires at least quadratic elements to be the constituents of the developed mesh and it was decided to use triangular elements for the whole domain.

A considerable number of these experimental points need to be projected on each element of the mesh, so the interpolated coefficients (located at the nodes) could have trustworthy results. Based on this concept, the elements should be big enough to encompass a significant amount of data points. On the other hand, the mesh should be fine enough to ensure that the geometry's shape and curvatures are preserved. Therefore, it can be noted that the generation of the elements' size heavily depends on how many measuring points were recorded with the DIC set-up.

After creating a mesh based on the density of experimental data, it was defined that the local coordinates  $\mathbf{e}_1$  and  $\mathbf{e}_2$  would be the principal curvature directions of the generated shell. These vector fields were computed via a multi-scale curvature estimation method (Panozzo *et al.*, 2010) and with the support of an open-source library for geometry processing named as LIBIGL (Jacobson *et al.*, 2017). The computation of the third direction  $\mathbf{e}_3$  was obtained by computing the normal direction of each element. At the end of this procedure, the local basis of unit vectors ( $\mathbf{e}_1, \mathbf{e}_2, \mathbf{e}_3$ ) was defined.

### C. Assessment of the global displacements and rotations

Not just the terms  $\mathbf{U}_{exp}^{h/2}$  and  $\mathbf{x}$  should be available at this point, but the spatial coordinates of the nodes of the mesh and the quadratic shape functions are also known. With all these terms at hand, one has all inputs of Eq. (27) and the global DoFs related to the displacement  $\tilde{\mathbf{U}}^{h/2}$  can be computed. Afterwards, the normal direction of the mesh under its deformed state  $\mathbf{n}_{def}$  was estimated with the purpose of extracting the missing global rotation  $\tilde{\mathbf{A}}$  through Eq. (28).

After storing the fields  $\tilde{\mathbf{U}}^{h/2}$  and  $\tilde{\mathbf{A}}$  at the nodes of the mesh and by having *a priori* knowledge of the local coordinates ( $\mathbf{e}_1, \mathbf{e}_2, \mathbf{e}_3$ ) of the shell, a change of basis vectors can be computed for each element as described in Sec. II E. By performing the change of basis of unit vectors, the fields  $\tilde{\mathbf{u}}^{h/2}$  and  $\tilde{\mathbf{a}}$  are made available.

### D. Data differentiation, mid-surface terms, generalized forces, and structural intensity

The terms  $\tilde{\mathbf{u}}^{h/2}$  and  $\tilde{\mathbf{a}}$  in combination with the quadratic shape functions are then used to compute these very fields and the required spatial derivatives at the elements' barycentric coordinates [Eqs. (30)–(32)]. The terms  $\mathbf{u}_{,i}^{h/2}$  and  $\mathbf{a}_{,i}$  are then used as inputs in Eqs. (9) and (10) to assess the strains  $\boldsymbol{\epsilon}^{h/2}$  and  $\boldsymbol{\chi}$ , while the term  $\mathbf{a}_{,ij}$  is used to compute  $\boldsymbol{\chi}_{,i}$  [Eq. (21)]. At the end of this process, the terms  $\boldsymbol{\epsilon}^{h/2}$ ,  $\boldsymbol{\chi}$  and  $\boldsymbol{\chi}_{,i}$  are available.

All terms at the right-hand side of Eqs. (22) and (23) should be available at this point and the displacement  $\mathbf{u}$  and strains  $\boldsymbol{\gamma}$  can be computed if *a priori* knowledge of the sample's thickness is known.

Since  $\boldsymbol{\gamma}$ ,  $\boldsymbol{\chi}$ ,  $\boldsymbol{\chi}_{,i}$  and the material properties of the membrane are at hand, Eqs. (14), (15), (18)–(20) can be used to access the generalized forces ( $\mathbf{Q}$ ,  $\mathbf{M}$ , and  $\mathbf{N}$ ). Finally, since the displacement  $\mathbf{u}$ , rotation  $\mathbf{a}$ , and generalized forces  $\mathbf{Q}$ ,  $\mathbf{M}$ , and  $\mathbf{N}$  are present, and by knowing the frequency in which the membrane is being excited, it is possible to compute and visualize the SI from Eqs. (1)–(4).

Apart from processing the displacements of a real structure, the validation of the proposed method was also tested on a FE-Method model and is presented in the Appendix of this paper. The SI intensity results that are directly acquired from the model were compared with the energy transmission that is obtained by following the proposed method.

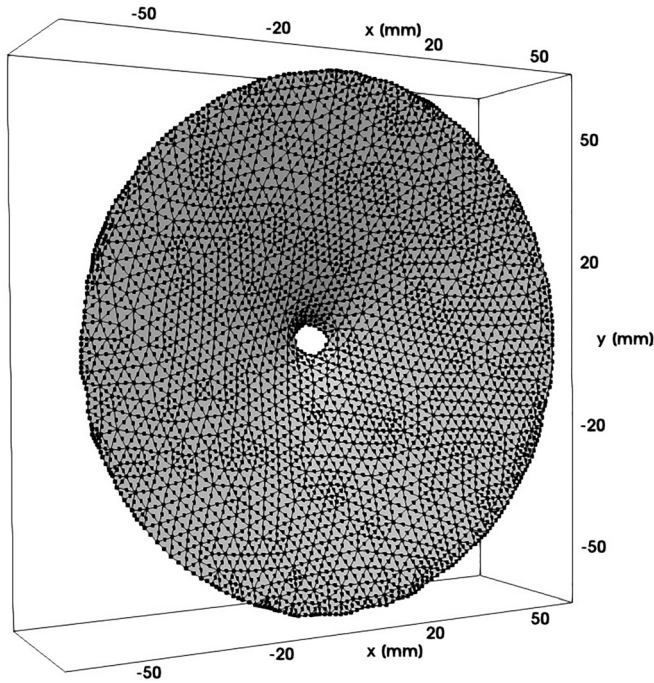


FIG. 2. FE mesh resembling the shape of the circular membrane (1.906 quadratic and flat elements and 3.964 nodes). The points depicted on the figure represent the nodes where the DoFs are stored.

## V. RESULTS

### A. Measurements via the DIC technique

After preparing the set-up described in Sec. III and setting the loudspeaker to excite the sample with harmonic excitations ranging from 60 to 170 Hz, the spatial coordinates  $\mathbf{x}$  and related global displacements  $\mathbf{U}_{exp}^{h/2}$  were processed by the Istra4D software. A total of 24.250 measurement points were correlated for every excitation frequency and a representation of this point cloud can be seen in Fig. 4(a).

As pointed out, the term  $\mathbf{U}_{exp}^{h/2}$  is dependent on the frequency at which the sample was excited. Since the same

displacement processing described in Sec. IV is repeated for every frequency, the intermediate steps towards the SI assessment are displayed next just for the recorded data at 130 Hz. At the end of this section, the computed SI vector fields of that very frequency and others within the mentioned range are also displayed.

### B. Mesh generation and definition of the local coordinate system

Since the DIC system provided the spatial coordinates of the membrane's outer-surface, it is feasible to develop a mesh whose shape resemble the original surface. As explained in Sec. IV, quadratic basis functions were used to describe the elements of the mesh, which, in turn, were chosen to be of the triangular type. Since a significant amount of data points were recorded, it was feasible to develop a mesh with elements that were relatively small but would still enclose a significant amount of data points. It was decided to build a mesh whose elements would encompass approximately 12 data points each, a number that would also ensure that the membrane's shape was preserved.

A mesh containing 3.964 nodes and 1.906 LST elements was generated, which can be seen in Fig. 2. It can also be noted from the same figure that the mesh was developed only on the regions where the shell theory is applicable, i.e., the free-zones of the sample where no thickness or stiffness heterogeneities are to be found.

After creating the mesh, one can define the local coordinates whose directions were used to compute the fields' spatial derivatives. By computing the principal curvature directions of the mesh with the LIBIGL library (Jacobson *et al.*, 2017), the basis vectors ( $\mathbf{e}_1$ ,  $\mathbf{e}_2$ ,  $\mathbf{e}_3$ ) were extracted. Figure 3 presents the tangent local coordinates, which are the guidelines for the spatial differentiations.

Last, the quality of the developed mesh was tested on the basis of a shell model, which is shown in the Appendix. From this validation, it was concluded that the developed mesh that follows the Kirchhoff-Love postulates was able to

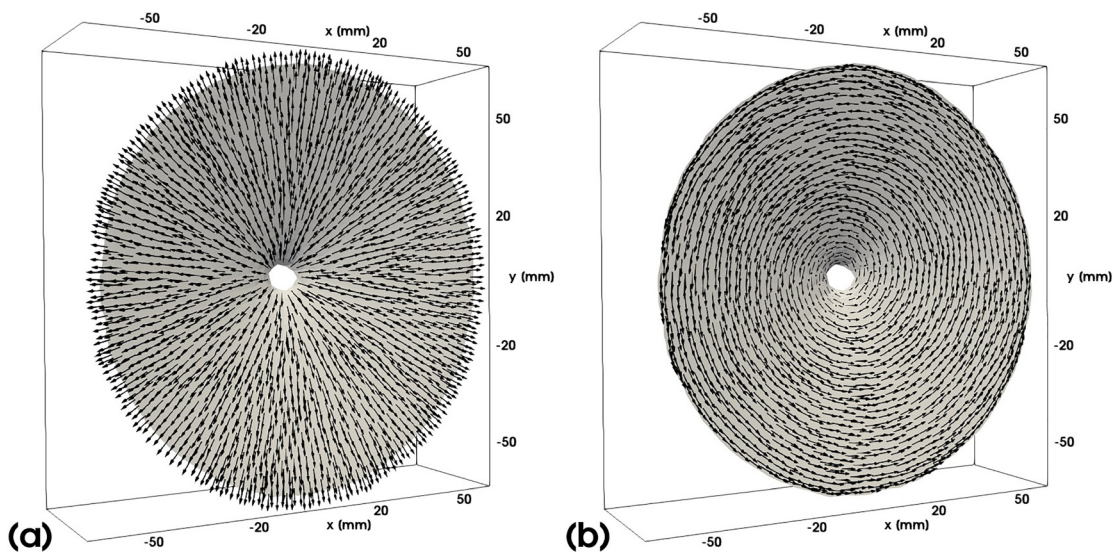


FIG. 3. (Color online) Representation of the shell's tangent local coordinates  $\mathbf{e}_1$  (a) and  $\mathbf{e}_2$  (b).

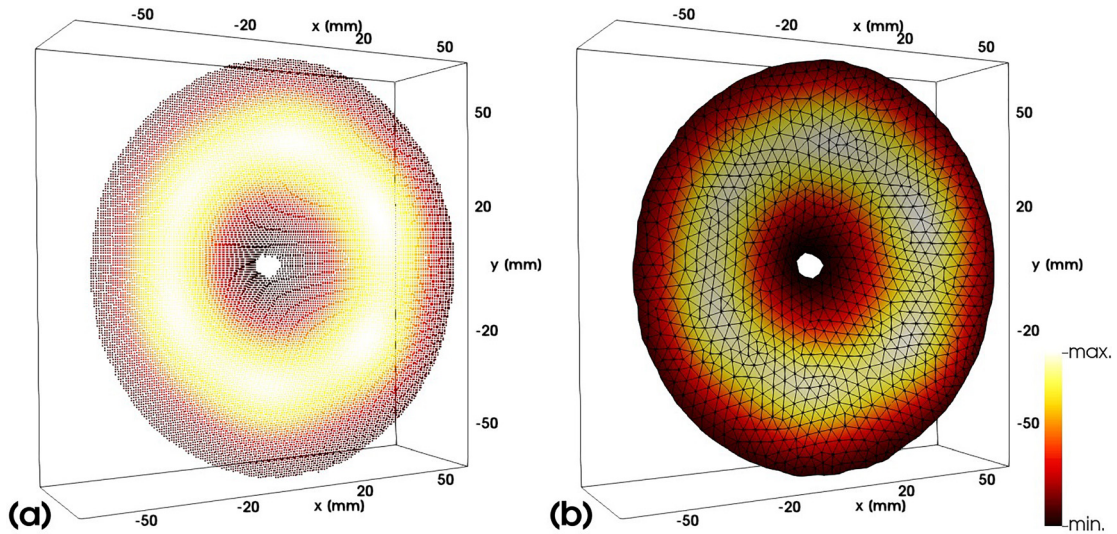


FIG. 4. (Color online) Projection of data from the dense point cloud to the quadratic mesh. (a) displays the term  $|\mathbf{U}_{exp}^{h/2}|$  on 24,250 measured points. (b) displays the projected displacements  $|\tilde{\mathbf{U}}^{h/2}|$  on the nodes of the mesh.

reproduce the SI results of the model. With this validation at hand, the FE mesh was used for further processing.

### C. Computation of global displacements and rotations

With the quadratic mesh, the displacement  $\mathbf{U}_{exp}^{h/2}$  and related positions  $\mathbf{x}$  at hand, Eq. (27) could be used to project the experimental data on the nodes of the mesh and the global displacement denoted as  $\tilde{\mathbf{U}}^{h/2}$  was computed. Figure 4 displays the magnitude of the global displacement before ( $|\mathbf{U}_{exp}^{h/2}|$ ) and after ( $|\tilde{\mathbf{U}}^{h/2}|$ ) the projection. The three global components of  $\tilde{\mathbf{U}}^{h/2}$  are also displayed separately in Fig. 5.

Since  $\tilde{\mathbf{U}}^{h/2}$  has been computed, one can calculate  $\mathbf{n}_{def}$  of the mesh under its deformed configuration, so the global

rotation  $\tilde{\mathbf{A}}$  can be assessed through Eq. (28). The magnitude and relative phase of the components of this term are presented in Fig. 6.

### D. Data processing

At this step, the mesh contains six global DoFs ( $\tilde{\mathbf{U}}^{h/2}$  and  $\tilde{\mathbf{A}}$ ) on each of its nodes (shown in Figs. 5 and 6) and the local coordinates ( $\mathbf{e}_1, \mathbf{e}_2, \mathbf{e}_3$ ) are also at hand (Fig. 3). By following the description shown in Sec. II E, the mentioned terms can be used to compute the local displacement and rotation, i.e.,  $\tilde{\mathbf{u}}^{h/2}$  or  $\tilde{\mathbf{a}}$ .

The estimation of these terms and their spatial derivatives are then computed at the barycentric coordinates of each element Eqs. (30)–(32). At the end of this process, the terms  $\mathbf{u}^{h/2}$ ,  $\mathbf{u}_{,i}^{h/2}$ , or  $\mathbf{a}$ ,  $\mathbf{a}_{,i}$ , and  $\mathbf{a}_{,ij}$  are available and, in turn,

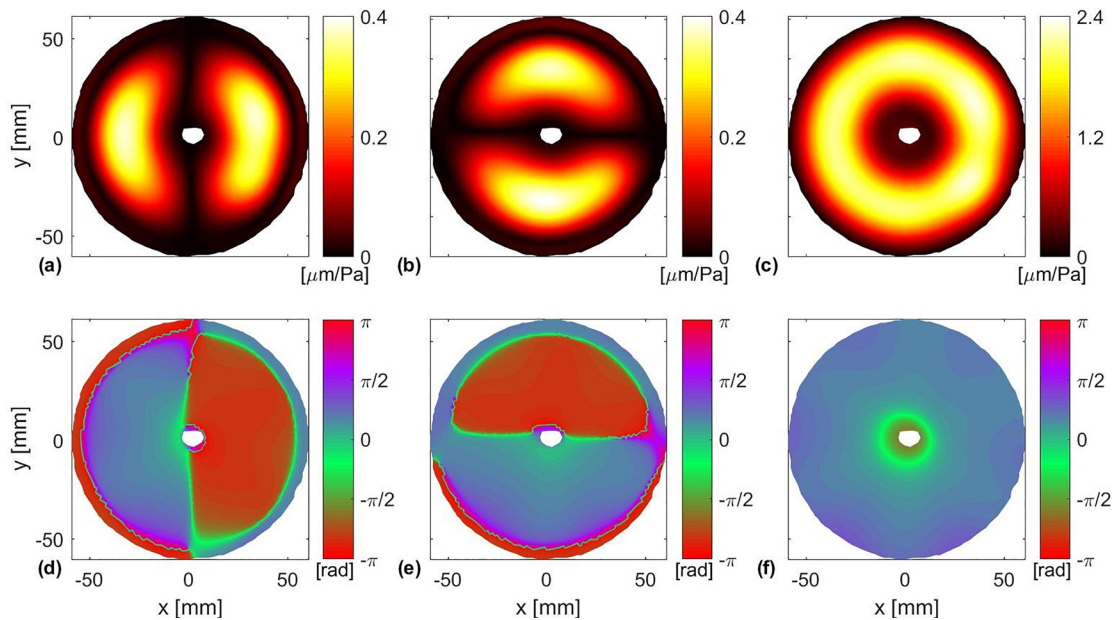


FIG. 5. (Color online) Components of the global displacement  $\tilde{\mathbf{U}}^{h/2}$  in the directions  $\mathbf{e}_x$  [(a), (d)],  $\mathbf{e}_y$  [(b), (e)], and  $\mathbf{e}_z$  [(c), (f)]. The first row [(a)–(c)] presents the absolute value of these components, while the second row [(d)–(f)] displays their relative phase with respect to the pressure excitation.

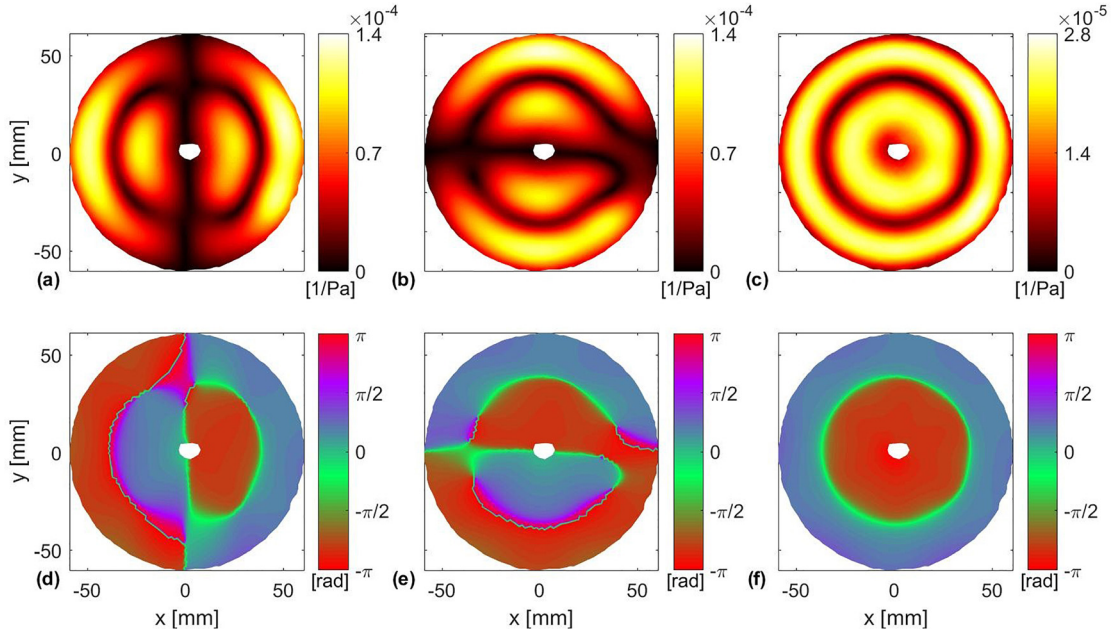


FIG. 6. (Color online) Components of the global rotation  $\bar{\mathbf{A}}$  in the directions  $\mathbf{e}_x$  [(a), (d)],  $\mathbf{e}_y$  [(b), (e)], and  $\mathbf{e}_z$  [(c), (f)].

the Green-Lagrange strain at the outer-surface  $\boldsymbol{\varepsilon}^{h/2}$  [Eq. (9)], bending curvature  $\boldsymbol{\chi}$  [Eq. (10)] and its first-order derivative  $\boldsymbol{\chi}_{,i}$  [Eq. (21)] can also be assessed.

The last step consists in using Eqs. (22) and (23) to assess the displacement  $\mathbf{u}$  and membrane strain  $\boldsymbol{\gamma}$  on the shell's mid-surface. All terms from both equations are presented in Figs. 7 [terms of Eq. (22)] and 8 [terms of Eq. (23)] with respect to the local coordinate  $\mathbf{e}_1$  as examples.

By having *a priori* knowledge of the membrane's material properties, the strains and related derivatives ( $\boldsymbol{\gamma}$ ,  $\boldsymbol{\chi}$ , and  $\boldsymbol{\chi}_{,i}$ ), all terms at the right-hand side of Eqs. (14) (15), and (18) are present and the shell's generalized forces ( $\mathbf{Q}$ ,  $\mathbf{N}$ , and  $\mathbf{M}$ ) are accessible. Moreover, since the terms  $\mathbf{u}$  and  $\mathbf{a}$  are also available, one has all the necessary components to

compute the SI  $\mathbf{I}$  from Eqs. (1)–(4). As examples, the magnitude of the individual SI contributions ( $\mathbf{I}_Q$ ,  $\mathbf{I}_M$ , and  $\mathbf{I}_N$ ) are presented in Fig. 9.

The processing of the shape and displacement data described above was repeated for the terms  $\mathbf{U}_{exp}^{h/2}$  recorded under all other excitation frequencies. Figure 10 displays the total SI vector field from displacement data, which were recorded at 60, 80, 130, and 170 Hz.

## VI. DISCUSSION AND CONCLUSIONS

From Fig. 10, it can be noted that the all SI vector fields contain energy transmission patterns that are qualitatively consistent with the built set-up. It can be noted that a strong

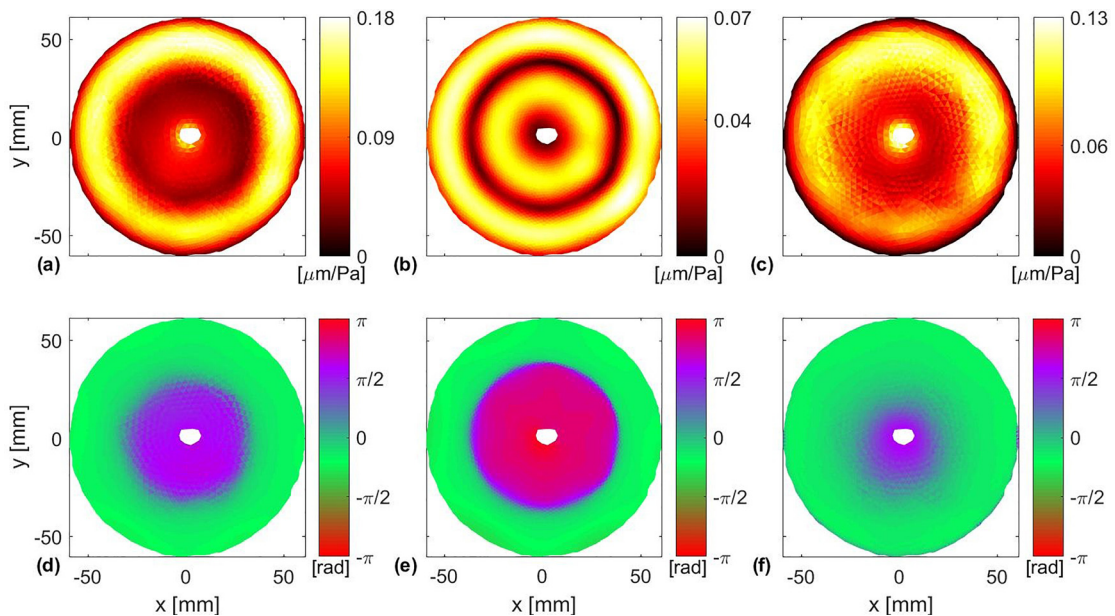


FIG. 7. (Color online) Representation of the terms of Eq. (22) from the direction  $\mathbf{e}_1$  after data processing. The displayed scalar data are  $u_1^{h/2}$  [(a), (d)],  $(h/2)a_1$  [(b), (e)], and  $u_1$  [(c), (f)].

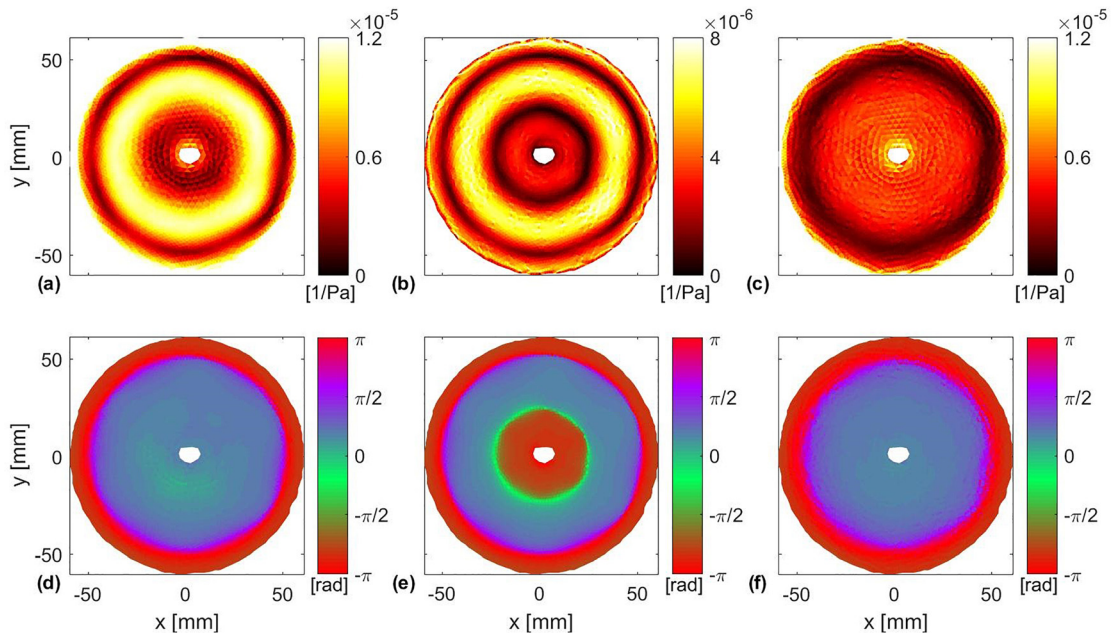


FIG. 8. (Color online) Representation of the terms of Eq. (23) from the direction  $\mathbf{e}_1$  after data processing. The displayed scalar data are  $\epsilon_{11}^{h/2}$  [(a), (d)],  $(h/2)\chi_{11}$  [(b), (e)], and  $\gamma_{11}$  [(c), (f)].

vector field convergence occurs on the region where the viscous polymer was installed. Interestingly, it is also worth noting that this convergence takes place through different transmission paths, which shows the strong dependence between the SI results and the excitation frequency.

By analyzing the individual contributions of energy transmission from the generalized forces at 130 Hz (Fig. 9), it could be seen that the component related to the membrane force was not just non-negligible, but it was, by far, the most important term for the energy transmission. The strong relation between the total SI and individual power contribution of the membrane force  $\mathbf{N}$  was present in all recorded frequencies and corroborates with the statement that axial waves need to be taken into account when irregular shells are being analyzed (Ventsel and Krauthammer, 2001).

Even though just experimental data from a sample's outer-surface are available, the proposed method could estimate SI results from the sample's mid-surface by invoking assumptions based on the Kirchhoff-Love postulates and

approximations regarding the mesh. Moreover, and to the authors' knowledge, the only works describing the SI assessment on shells require the principle curvatures of the sample to be aligned with analytical coordinate systems, such as the study on a cylindrical shell presented in Williams (1991). This is not the case for the strategy described in this work, which is applicable to shells with arbitrary shape configurations. Moreover, the data differentiation via FE basis functions was not common in works related to the study of energy flow. The most well-known techniques to compute spatial derivatives are either through the finite difference method (Arruda and Mas, 1998; Schmidt, 2009) or by processing the fields in the wavenumber domain (Arruda, 1992; Lopes et al., 2006; Morikawa et al., 1996; Pascal et al., 1996; Pascal et al., 2002; Pascal et al., 2006).

The proposed method showed reliable results when the energy transmission paths and their quantitative contributions were compared with the SI presented in a shell model (shown in the Appendix). It is also worth noting that the

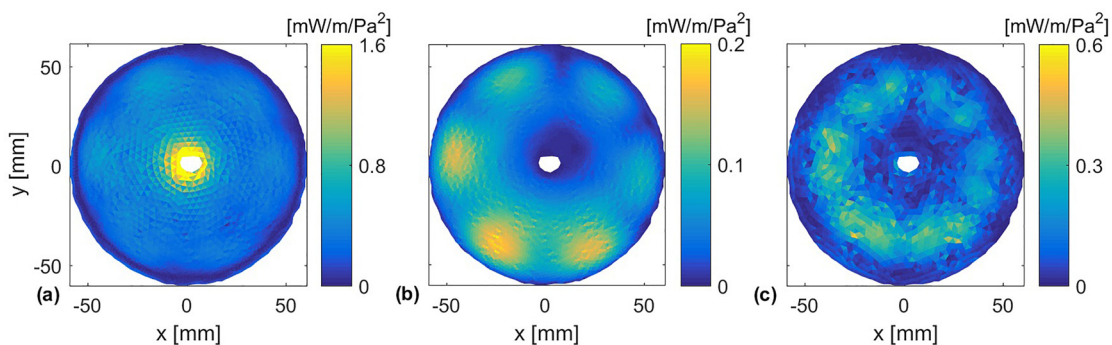


FIG. 9. (Color online) Individual contributions of the energy transmission taking place on the circular membrane at 130 Hz: the presented data are the normalized values of  $|\mathbf{I}_N|$  (a),  $|\mathbf{I}_M|$  (b), and  $|\mathbf{I}_O|$  (c).

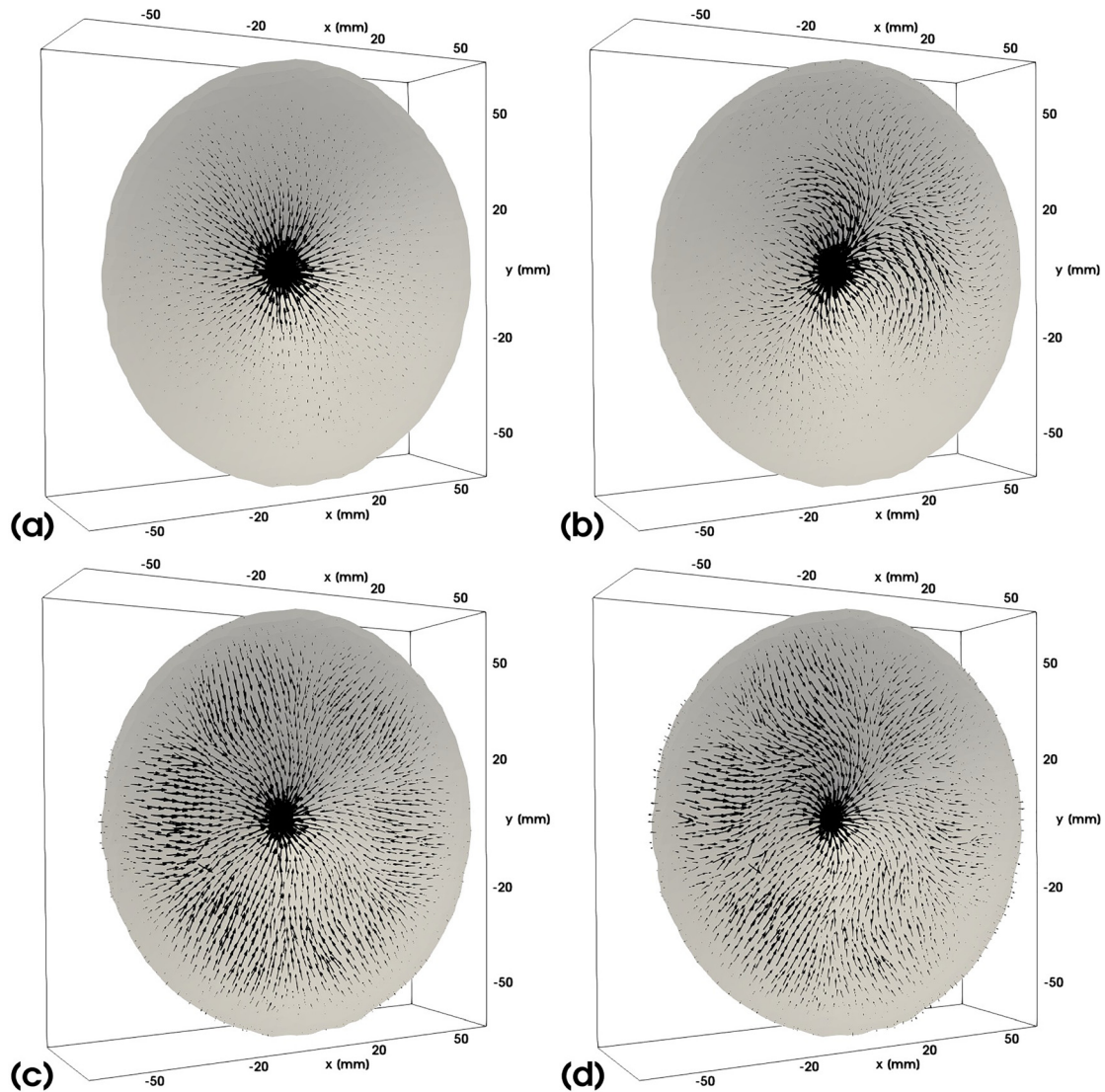


FIG. 10. (Color online) Structural Intensity vector fields [Eq. (1)] taking place on the circular membrane at 60 (a), 80 (b), 130 (c), and 170 Hz (d).

mentioned model was based on the Mindlin-Reissner theory, while the proposed method is built upon the Kirchhoff-Love plate model. Even though the latter neglects the curvatures and shear strains for the individual elements, the estimated SI converged towards the real numerical solution as it can be noted in Figs. 12(c) and 12(d) and Fig. 13.

By knowing that the proposed approach preserves the information regarding the SI, it can be stated that this procedure is reliable to estimate the strains and the energy transmission on the mid-surface just with the displacements on the outer-surface at hand. Therefore, due to the validation of this work via a shell model and to the results shown in Figs. 9 and 10, it can be said that the strategy to project experimental data via the FE approximation in combination with data differentiation via quadratic shape functions showed to be a meaningful approach to assess transmission paths of arbitrary shells.

#### ACKNOWLEDGMENTS

Financial support for this work was supplied by the Research Foundation of Flanders (FWO), (Grant No. G049414N).

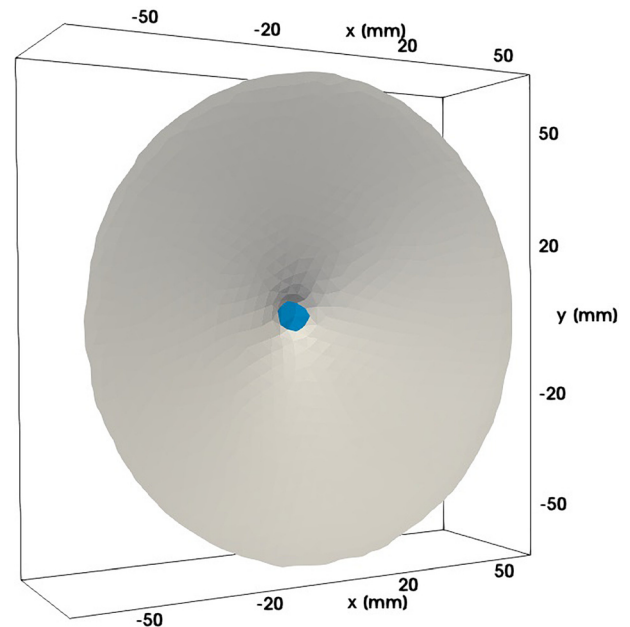


FIG. 11. (Color online) Representation of the model's geometry developed for validation.

## APPENDIX: VALIDITY OF THE STRUCTURAL INTENSITY ASSESSMENT

A shell model that follows the Mindlin-Reissner theory was created in a FE-Method software (COMSOL<sup>®</sup> Multiphysics 5.2 a, Burlington, MA) and is represented in Fig. 11. The geometry was generated on the basis of the point cloud  $\mathbf{x}$  shown in Fig. 4(a).

Since the purpose of this model is to validate the method described in Sec. IV, it was decided to export the numerical displacement data in such a way that it would resemble the experimental  $\mathbf{U}_{exp}^{h/2}$  described in Sec. V A. To mimic the densely populated measurement points, a refined mesh containing 19,615 nodes was generated over the geometry shown in Fig. 11.

The nodes located at the circumference of this model were clamped, a viscous damper of  $1 \text{ N} \cdot \text{s/m}$  was applied at the center of the membrane to simulate the viscous effects of the polymer strip (blue elements shown in Fig. 11), and a uniform and harmonic pressure at 100 Hz was applied on the

geometry's free-zones to mimic the harmonic excitation. Last, the material properties and thickness of the shell model were set to be the equal to the ones provided in Sec. III.

The results provided by the model are shown in the first column of Fig. 12. Figure 12(a) displays the numerical displacement located at the nodes of the mesh and Fig. 12(c) shows the related SI vector fields. From here, one can compare the original SI results of Fig. 12(c) with the energy transmission that can be estimated through the process described in Sec. IV.

First, the global displacements located at the nodes of this model [Fig. 12(a)] were exported and Eq. (27) was used to project the global displacement field on the mesh shown in Fig. 2. A representation of this projection can be seen in Fig. 12(b). By following the data processing shown in Sec. IV, the total SI could be assessed and visualized [Fig. 12(d)]. By comparing the energy transmission of the model [Fig. 12(c)] and the processed SI from the proposed method [Fig. 12(d)], it can be noticed that both vector fields have similar paths over the geometry's domain.

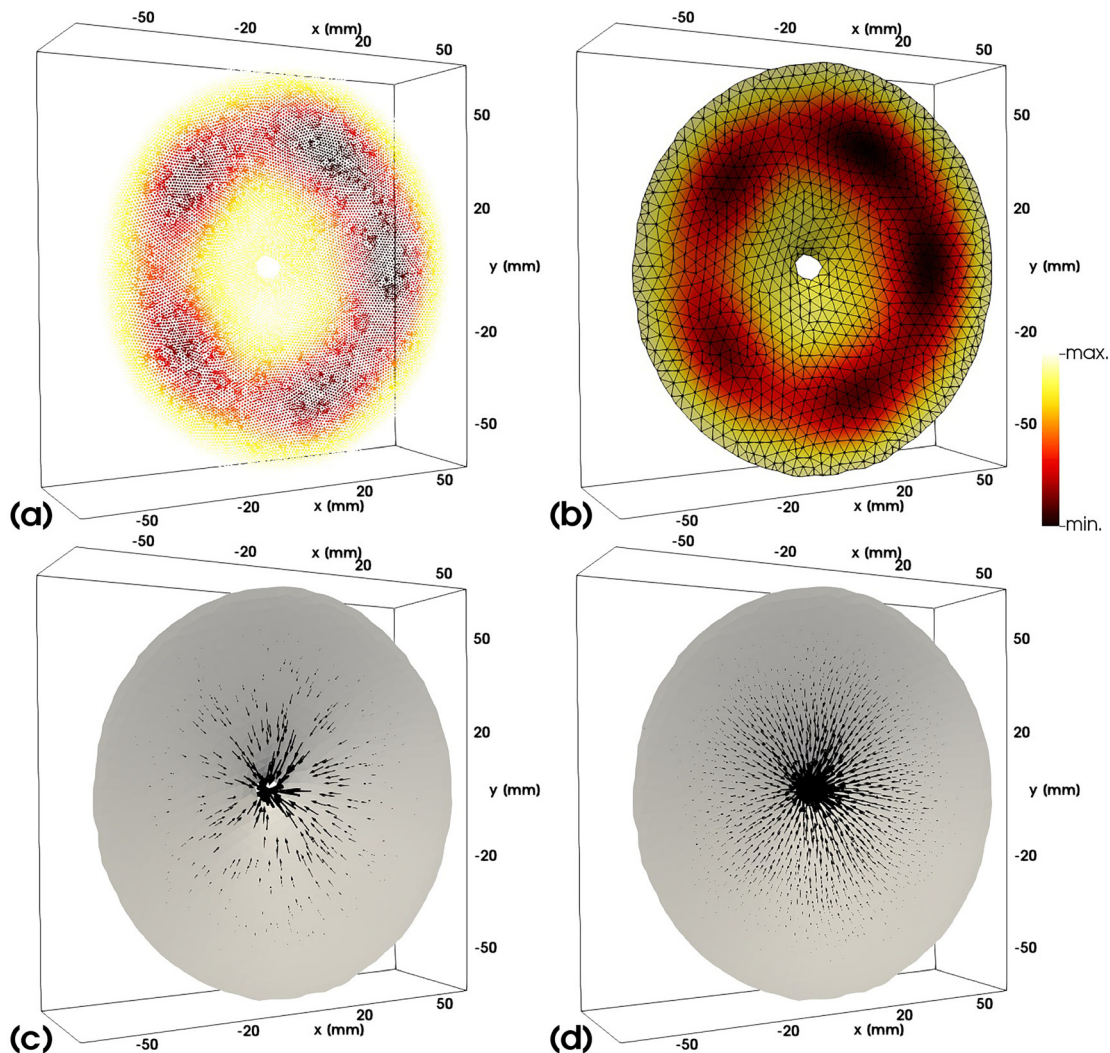


FIG. 12. (Color online) Representation of displacement data [(a), (b)] and SI [(c), (d)]. The terms displayed on the first column [(a), (c)] were obtained from the FE software and are directly acquirable after the simulation's conclusion. The second column [(b), (d)] displays the same terms that can be visualized on the basis of the method presented in Sec. IV.

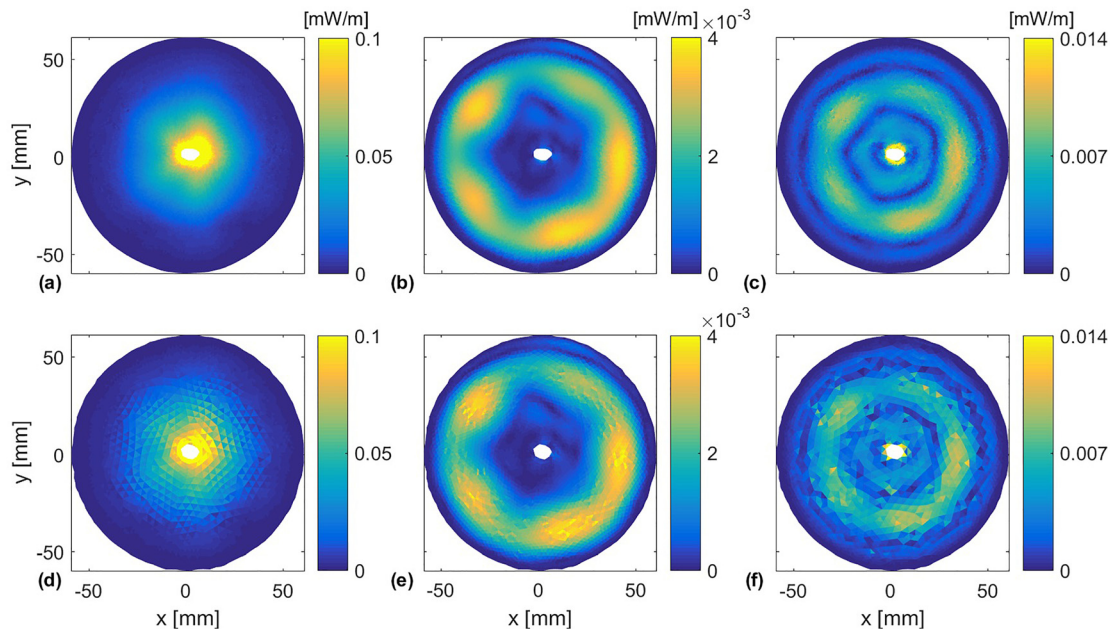


FIG. 13. (Color online) Individual contributions of the energy transmission taking place on the model: the presented data are values of  $|\mathbf{I}_N|$  (a, d),  $|\mathbf{I}_M|$  (b, e), and  $|\mathbf{I}_Q|$  (c, f). The first row displays these fields that were computed via the COMSOL model. The second row shows the SI contributions, which were processed via the proposed method.

The SI contributions of the membrane forces  $\mathbf{I}_N$ , bending moments  $\mathbf{I}_M$  and shear forces  $\mathbf{I}_Q$  of the model can also be analyzed separately. The first row of Fig. 13 displays the absolute value of these vector fields. The second row of the same figure displays these very values from the SI shown in Fig. 12(d), i.e., the energy flow computed via the proposed method.

By comparing the fields that were directly computed from the COMSOL model [Figs. 13(a)–13(c)] with the ones calculated on the basis of the Kirchhoff-Love plate model [Figs. 13(d)–13(f)], it can be noted that they are quantitatively consistent with each other. Due to this comparison, it can be stated that the proposed method not just computes the energy paths taking place on a shell [Fig. 12(d)], but also preserves the SI magnitudes [Figs. 13(d)–13(f)], despite the stronger assumptions being imposed on the Kirchhoff-Love plate model.

Al Ba'ba'a, H. B., Attarzadeh, M. A., and Nouh, M. (2018). "Experimental evaluation of structural intensity in 2D plate-type locally resonant elastic metamaterials," *J. Appl. Mech.* **85**, 041005.

Al Ba'ba'a, H. B., and Nouh, M. (2017). "Mechanics of longitudinal and flexural locally resonant elastic metamaterials using a structural power flow approach," *Int. J. Mech. Sci.* **122**, 341–354.

Arruda, J. F. (1992). "Surface smoothing and partial spatial derivatives computation using a regressive discrete Fourier series," *Mech. Syst. Signal Process.* **6**(1), 41–50.

Arruda, J. F., and Mas, P. (1998). "Localizing energy sources and sinks in plates using power flow maps computed from laser vibrometer measurements," *Shock Vib.* **5**(4), 235–253.

Avril, S., Feissel, P., Pierron, F., and Villon, P. (2009). "Comparison of two approaches for differentiating full-field data in solid mechanics," *Meas. Sci. Technol.* **21**(1), 015703.

Avril, S., and Pierron, F. (2007). "General framework for the identification of constitutive parameters from full-field measurements in linear elasticity," *Int. J. Solids Struct.* **44**(14–15), 4978–5002.

Bischoff, M., and Ramm, E. (1997). "Shear deformable shell elements for large strains and rotations," *Int. J. Numer. Methods Eng.* **40**(23), 4427–4449.

Büchter, N., Ramm, E., and Roehl, D. (1994). "Three-dimensional extension of non-linear shell formulation based on the enhanced assumed strain concept," *Int. J. Numer. Methods Eng.* **37**(15), 2551–2568.

Chappelle, D., and Bathe, K.-J. (2010). *The Finite Element Analysis of Shells-Fundamentals* (Springer Science & Business Media, New York).

Cho, D.-S., Choi, T.-M., Kim, J.-H., and Vladimir, N. (2016). "Structural intensity analysis of stepped thickness rectangular plates utilizing the finite element method," *Thin-Walled Struct.* **109**, 1–12.

Cho, D.-S., Choi, T.-M., Kim, J.-H., and Vladimir, N. (2018). "Dominant components of vibrational energy flow in stiffened panels analysed by the structural intensity technique," *Int. J. Naval Archit. Ocean Eng.* **10**, 583–595.

Cho, D.-S., Kim, K.-S., and Kim, B.-H. (2010). "Structural intensity analysis of a large container carrier under harmonic excitations of propulsion system," *Int. J. Naval Archit. Ocean Eng.* **2**(2), 87–95.

Dhatt, G., Marcotte, L., and Matte, Y. (1986). "A new triangular discrete Kirchhoff plate/shell element," *Int. J. Numer. Methods Eng.* **23**(3), 453–470.

Eck, T., and Walsh, S. J. (2012). "Measurement of vibrational energy flow in a plate with high energy flow boundary crossing using electronic speckle pattern interferometry," *Appl. Acoust.* **73**(9), 936–951.

Feng, Z., and Rowlands, R. (1991). "Smoothing finite-element and experimental hybrid technique for stress analyzing composites," *Comput. Struct.* **39**(6), 631–639.

Gavrić, L., and Pavić, G. (1993). "A finite element method for computation of structural intensity by the normal mode approach," *J. Sound Vib.* **164**(1), 29–43.

Hambric, S. A. (1990). "Power flow and mechanical intensity calculations in structural finite element analysis," *J. Vib. Acoust.* **112**(4), 542–549.

Hambric, S. A., and Szwer, R. P. (1999). "Predictions of structural intensity fields using solid finite elements," *Noise Control Eng. J.* **47**(6), 209–217.

Jacobson, A., Panozzo, D., et al. (2017). "libigl: A simple C++ geometry processing library," <http://libigl.github.io/libigl/> (Last viewed 1/6/2018).

Kraus, H. (1967). *Thin Elastic Shells* (John Wiley & Sons, New York).

Lamberti, A., and Semperlotti, F. (2013). "Detecting closing delaminations in laminated composite plates using nonlinear structural intensity and time reversal mirrors," *Smart Mater. Struct.* **22**(12), 125006.

- Lee, H., Lim, S., and Khun, M. (2006). "Diversion of energy flow near crack tips of a vibrating plate using the structural intensity technique," *J. Sound Vib.* **296**(3), 602–622.
- Li, Y., and Lai, J. (2000). "Prediction of surface mobility of a finite plate with uniform force excitation by structural intensity," *Appl. Acoust.* **60**(3), 371–383.
- Liu, Z., Lee, H., and Lu, C. (2005). "Structural intensity study of plates under low-velocity impact," *Int. J. Impact Eng.* **31**(8), 957–975.
- Lopes, H., Guedes, R. M., and Vaz, M. (2006). "Techniques in numerical differentiation of experimentally noisy data," in *Proceedings of the 5th International Conference of Mechanical & Materials in Design*, July 24–26, Porto, Portugal, pp. 27–28.
- Miguel, C. J., and Feit, D. (1986). *Sound, Structures, and Their Interaction* (MIT Press, Cambridge, MA).
- Morikawa, R., Ueha, S., and Nakamura, K. (1996). "Error evaluation of the structural intensity measured with a scanning laser doppler vibrometer and AK-space signal processing," *J. Acoust. Soc. Am.* **99**(5), 2913–2921.
- Morse, P. M., and Feshbach, H. (1946). *Methods of Theoretical Physics* (Technology Press, New York).
- Murthy, S., and Gallagher, R. (1986). "A triangular thin-shell finite element based on discrete Kirchhoff theory," *Comput. Methods Appl. Mech. Eng.* **54**(2), 197–222.
- Noiseux, D. (1970). "Measurement of power flow in uniform beams and plates," *J. Acoust. Soc. Am.* **47**(1B), 238–247.
- Novozhilov, V. V. (1959). *Thin Shell Theory* (P. Noordhoff, Amsterdam, the Netherlands).
- Panozzo, D., Puppo, E., and Rocca, L. (2010). "Efficient multi-scale curvature and crease estimation," in *Proceedings of the 2nd International Workshop on Computer Graphics, Computer Vision and Mathematics*, GraVisMa 2010, September 7–10, Brno, Czech Republic.
- Pascal, J.-C., Carniel, X., Chalvidan, V., and Smigielski, P. (1996). "Determination of phase and magnitude of vibration for energy flow measurements in a plate using holographic interferometry," *Opt. Lasers Eng.* **25**(4–5), 343–360.
- Pascal, J.-C., Carniel, X., and Li, J.-F. (2006). "Characterisation of a dissipative assembly using structural intensity measurements and energy conservation equation," *Mech. Syst. Signal Process.* **20**(6), 1300–1311.
- Pascal, J.-C., Li, J.-F., and Carniel, X. (2002). "Wavenumber processing techniques to determine structural intensity and its divergence from optical measurements without leakage effects," *Shock Vib.* **9**(1–2), 57–66.
- Pascal, J.-C., Loyau, T., and Mann, J. III. (1990). "Structural intensity from spatial fourier transformation and bahim acoustical holography method," in *Proceedings of the Congress on Structural Intensity and Vibrational Energy Flow*, August 27–29, Senlis, France, pp. 197–204.
- Pavić, G. (1976). "Measurement of structure borne wave intensity, Part I: Formulation of the methods," *J. Sound Vib.* **49**(2), 221–230.
- Petrone, G., De Vendittis, M., De Rosa, S., and Franco, F. (2016). "Numerical and experimental investigations on structural intensity in plates," *Compos. Struct.* **140**, 94–105.
- Pires, F., Muyschondt, P., Keustermans, W., Vanlanduit, S., Roozen, N., and Dirckx, J. (2018). "Structural intensity analysis of flat plates based on digital stroboscopic holography measurements," *J. Sound Vib.* **428**, 168–178.
- Romano, A. J., Abraham, P. B., and Williams, E. G. (1990). "A poynting vector formulation for thin shells and plates, and its application to structural intensity analysis and source localization. Part I: Theory," *J. Acoust. Soc. Am.* **87**(3), 1166–1175.
- Romano, A. J., Williams, E., Russo, K., and Schuette, L. (1992). "On the visualization and analysis of fluid-structure interaction from the perspective of instantaneous intensity," *J. Phys.* **IV** 2(C1), C1-597–C1-600.
- Roozen, N., Guyader, J., and Glorieux, C. (2015). "Measurement-based determination of the irrotational part of the structural intensity by means of test functional series expansion," *J. Sound Vib.* **356**, 168–180.
- Saijyou, K. (2007). "Measurement of structural intensity using boundary element method-based nearfield acoustical holography," *J. Acoust. Soc. Am.* **121**(6), 3493–3500.
- Schaal, C., Ebert, J., Bös, J., and Melz, T. (2016). "Relation between structural intensity-based scalars and sound radiation using the example of plate-rib models," *J. Vib. Acoust.* **138**(4), 041011.
- Schmidt, W. T. (2009). "Open-crack damage assessments of aluminum panels using structural intensity-based techniques," Ph.D. thesis, The Pennsylvania State University, State College, PA.
- Schreier, H., Orteu, J.-J., and Sutton, M. A. (2009). *Image Correlation for Shape, Motion and Deformation Measurements* (Springer, New York).
- Semperlotti, F., and Conlon, S. C. (2010). "Structural damage identification in plates via nonlinear structural intensity maps," *J. Acoust. Soc. Am.* **127**(2), EL48–EL53.
- Shepherd, M. R., Conlon, S. C., Semperlotti, F., and Hambric, S. A. (2012). "Structural intensity modeling and simulations for damage detection," *J. Vib. Acoust.* **134**(5), 051004.
- Tian, X., Liu, G., Gao, Z., Chen, P., and Mu, W. (2017). "Crack detection in offshore platform structure based on structural intensity approach," *J. Sound Vib.* **389**, 236–249.
- Tran, T., Lee, H., and Lim, S. (2007). "Structural intensity analysis of thin laminated composite plates subjected to thermally induced vibration," *Compos. Struct.* **78**(1), 70–83.
- Ventsel, E., and Krauthammer, T. (2001). *Thin Plates and Shells: Theory, Analysis, and Applications* (CRC Press, Boca Raton, FL).
- Vuye, C. (2011). "Measurement and modeling of sound and vibration fields using a scanning laser doppler vibrometer," Ph.D. thesis, Vrije Universiteit Brussel, Brussels, Belgium.
- Wagner, W., and Gruttmann, F. (1994). "A simple finite rotation formulation for composite shell elements," *Eng. Comput.* **11**(2), 145–176.
- Williams, E. G. (1991). "Structural intensity in thin cylindrical shells," *J. Acoust. Soc. Am.* **89**(4), 1615–1622.
- Xu, X., Lee, H., and Lu, C. (2004a). "Numerical study on energy transmission for rotating hard disk systems by structural intensity technique," *Int. J. Mech. Sci.* **46**(4), 639–652.
- Xu, X., Lee, H., and Lu, C. (2004b). "The structural intensities of composite plates with a hole," *Compos. Struct.* **65**(3–4), 493–498.
- Xu, X., Lee, H., and Lu, C. (2005). "Power flow paths in stiffened plates," *J. Sound Vib.* **282**(3–5), 1264–1272.
- Zhang, Y. (1993). "An experimental method for structural intensity and source location," Ph.D. thesis, Iowa State University, Ames, Iowa.
- Zhang, Y., and Mann J. A. III. (1996). "Examples of using structural intensity and the force distribution to study vibrating plates," *J. Acoust. Soc. Am.* **99**(1), 354–361.
- Zienkiewicz, O. C., Taylor, R. L., Zienkiewicz, O. C., and Taylor, R. L. (1977). *The Finite Element Method* (McGraw-Hill, New York).